

## Three-Dimensional Measurement of Magnetic Moment Vectors Using Electron Magnetic Chiral Dichroism at Atomic Scale

Dongsheng Song<sup>1,2,\*</sup> and Rafal E. Dunin-Borkowski<sup>1</sup>

<sup>1</sup>*Ernst Ruska-Centre for Microscopy and Spectroscopy with Electrons and Peter Grünberg Institute, Forschungszentrum Jülich, 52425 Jülich, Germany*

<sup>2</sup>*Information Materials and Intelligent Sensing Laboratory of Anhui Province, Key Laboratory of Structure and Functional Regulation of Hybrid Materials of Ministry of Education, Institutes of Physical Science and Information Technology, Anhui University, Hefei 230601, China*

 (Received 23 February 2021; accepted 29 July 2021; published 19 August 2021)

Here we have developed an approach of three-dimensional (3D) measurement of magnetic moment vectors in three Cartesian directions using electron magnetic chiral dichroism (EMCD) at atomic scale. Utilizing a subangstrom convergent electron beam in the scanning transmission electron microscopy (STEM), beam-position-dependent chiral electron energy-loss spectra (EELS), carrying the EMCD signals referring to magnetization in three Cartesian directions, can be obtained during the scanning across the atomic planes. The atomic resolution EMCD signals from all of three directions can be separately obtained simply by moving the EELS detector. Moreover, the EMCD signals can be remarkably enhanced using a defocused electron beam, relieving the issues of low signal intensity and signal-to-noise-ratio especially at atomic resolution. Our proposed method is compatible with the setup of the widely used atomic resolution STEM-EELS technique and provides a straightforward way to achieve 3D magnetic measurement at atomic scale on newly developing magnetic-field-free TEM.

DOI: [10.1103/PhysRevLett.127.087202](https://doi.org/10.1103/PhysRevLett.127.087202)

Investigating three-dimensional (3D) magnetism is critical to understand the magnetic physics and properties of magnetic materials. At present, the most powerful tomographic techniques through x-ray [1,2] or transmission electron microscopy (TEM) [3–6] are able to experimentally map the magnetization or induction in 3D space with nanometer resolution, though it is still very tough associating with several typical issues, e.g., the challenge of tomographic data acquisition on instruments with special design, the complexity of magnetization reconstruction algorithms and the demanding for quantitative magnetic information. However, 3D measurement of magnetism at atomic scale is still not feasible.

Electron magnetic chiral dichroism (EMCD) utilizes an electron beam to measure magnetism in the TEM. Since its first proposal in 2003 [7] and experimental realization in 2006 [8], the spatial resolution has been significantly improved ranging from nanometer [9–15] to atomic scale [16–24]. Based on the EMCD sum rules [25–29], the element-selective spin and orbital magnetic moments could be calculated from the experimental EMCD signals. Moreover, EMCD has been developed to measure both in-plane and out-of-plane magnetization [30,31] without a series of specimen tilting in contrast to these 3D tomographic techniques [1,3–6]. Note that it leads to reduction of the measurement from 3D full-space to lateral plane for EMCD meanwhile. These achievements stimulate us to develop an approach of 3D EMCD measurement at atomic resolution.

Here, we have introduced the EMCD technique to measure the magnetic moments in all three Cartesian directions at laterally atomic resolution simply implemented on the aberration corrected scanning TEM (STEM) with electron energy-loss spectra (EELS). The simulations show that EMCD signals referring to all of the three magnetic components can be measured just by shifting the detector during the STEM-EELS acquisition. The signal delocalization analysis confirms the validity of atomic resolution. Moreover, using a defocused electron beam, the EMCD signals can be remarkably enhanced to relieve it of its notoriously low signal intensity and signal-to-noise-ratio (SNR).

The schematic diagram of atomic resolution EMCD for 3D magnetic measurement is shown in Fig. 1. First, the magnetic specimen is tilted to three-beam orientation, adopting the commonly used EMCD diffraction geometry. The magnetic components in three Cartesian directions are schematically indicated for the specimen. The atomic-sized electron beam with a certain convergence semi-angle (CA)  $\alpha$  is scanning across the atomic planes in real space. The elastically scattered electrons passing through the specimen are collected by a high angle annular dark field (HAADF) detector to image the atomic structure. The inelastically scattered electrons after the electron transitions are collected by the post column EEL spectrometer. In the diffraction plane, the simulated distributions of EMCD signals for out-of-plane and in-plane magnetization are

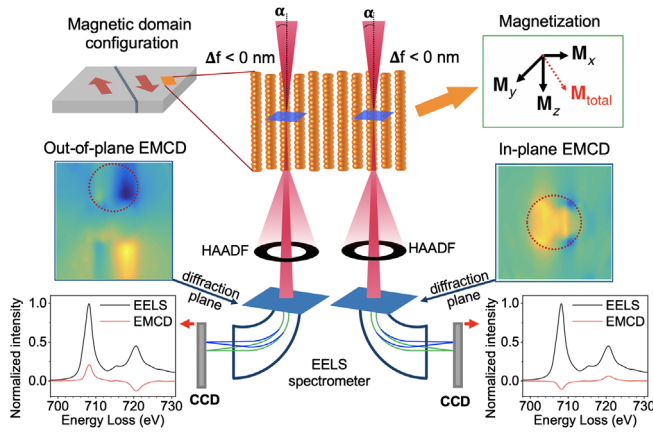


FIG. 1. Proposal to measure magnetic vectors in three directions by EMCD at atomic scale based on the STEM-EELS setup using a defocused and convergent electron beam. The magnetic sample is tilted to the three-beam orientation. The atomic sized electron beam is scanning across the atomic planes. The atomic structure can be imaged by the HAADF detector. The simulated EMCD signals both for in-plane and out-of-plane magnetization are shown in the diffraction plane. The EELS detector is marked with dotted red circles. The chiral EELS signals carrying 3D EMCD signals are acquired by the EEL spectrometer for further extraction of EMCD signals from a single atom plane.

displayed on each side of Fig. 1, respectively. By shifting the EELS detector to specific positions as indicated with dotted red circles, the chiral EELS signals carrying EMCD signals corresponding to magnetization in different directions can be acquired. At last, 3D EMCD signals for a single atomic plane can be extracted and the magnetic parameters can be further calculated. It should be noted that the conventional EMCD is always conducted in the TEM mode, for which a strong magnetic field of approximately 2 T will saturate the magnetic specimen along the electron beam direction (out-of-plane) [31]. For atomic resolution 3D EMCD measurement, atomic resolution microscope with a magnetic-field-free environment is needed, which has already been developed recently even if it has been only demonstrated for atomic structure imaging until now [32].

Based on the setup in Fig. 1, EMCD simulations are first conducted taking the example of *bcc* Fe under (200) three-beam orientation with the accelerating voltage ( $V$ ) of 300 kV and the thickness ( $t$ ) of 10.47 nm. The atomic model is shown in Fig. 2(a) by cutting the orthogonal supercell with [016] along the electron beam direction and  $\mathbf{G} = [200]$  along the  $x$  axis. The simulations are based on MATS v2 software using the combined multislice and Bloch-wave method [33,34]. The details for the descriptions of EMCD signals, simulation procedures, and parameters can be found in the Supplemental Material [35]. The momentum-resolved inelastic electron scattering cross section in the diffraction plane, including the nonmagnetic component in Fig. 2(b) and magnetic EMCD components for three Cartesian directions in Figs. 2(c) and 2(d), are

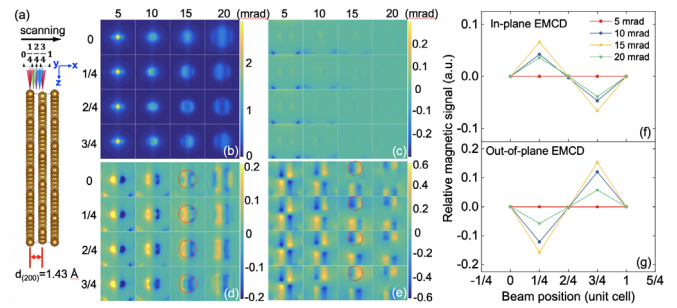


FIG. 2. Atomic resolution EMCD for 3D magnetic measurement. (a) Atomic model of *bcc* Fe under (200) three-beam orientation. The beam is scanning across the atomic plane at the positions of  $0$ ,  $d/4$ ,  $2d/4$ ,  $3d/4$ , and  $1d$ .  $d$  is the lattice spacing of (200) planes. Simulated distributions of the nonmagnetic signals (b) and the relative intensity of EMCD signals (c)–(e) in three Cartesian directions, respectively, at  $V = 300$  kV and  $t = 10.47$  nm at different convergence semi-angles. The red circles indicate the positions of the EELS detector for signal acquisition. The range of the diffraction plane is  $\pm 50$  mrad by  $\pm 50$  mrad. (f),(g) Atomic resolved in-plane ( $y$ ) and out-of-plane ( $z$ ) EMCD signals extract from the EELS detectors as a function of beam position. The difference of signals at  $d/4$  and  $-d/4$  ( $3d/4$ ) is the EMCD signal from a single atomic plane.

separately simulated at different CAs as a function of electron beam positions. The electron beam is scanned across the atomic plane in the [200] direction ( $x$  axis), respectively. The magnetization is set to one in all three directions in the simulations. The EMCD signals from  $x$  direction are negligible in Fig. 2(c) attributing to the small component of momentum transfer  $\mathbf{q}_y$  and  $\mathbf{q}_z$  under the three-beam orientation [30,31]. Nevertheless, the EMCD signals from the  $x$  direction can be achieved just simply by tilting the sample to its perpendicular direction, e.g., [020] three-beam orientation.

At CA = 5 mrad, for which the electron beam is not narrow enough to resolve the adjacent atomic plane, the nonmagnetic and EMCD signals are not varied during the movement of the electron beam. Above the atomic resolution limit for CA = 10, 15, and 20 mrad, the position dependent nonmagnetic and EMCD signals can be obviously observed. At the beam positions of  $0$  (on the atomic plane) and  $2d/4$  (in the middle of two atomic planes), the distribution of EMCD signals in the  $y$  and  $z$  directions are antisymmetric in the left-right half of the diffraction plane. However, at the beam positions of  $d/4$  and  $-d/4$  ( $3d/4$ ), the antisymmetric distributions of EMCD signals are broken with respect to the  $y$  axis in Figs. 2(d) and 2(e). Moreover, the EMCD signals at  $d/4$  and  $-d/4$  ( $3d/4$ ) positions show the mirror symmetry with the addition of a negative sign, owing to the mirror symmetry of beam positions with respect to the atomic plane in real space. Consequently, the atomic resolution 3D EMCD measurement can be achieved by taking advantage of these symmetries induced by beam positions.

An *off-axis* detector centered on the  $y$  axis [16], as indicated in Fig. 2(e), can provide a modulation of out-of-plane EMCD signals as shown in Fig. 2(g). More importantly, as the in-plane EMCD signals are mostly localized around the transmitted beam in Fig. 2(d), an *on-axis* detector will be favorable to provide a modulation of in-plane EMCD signals as shown in Fig. 2(f), for which the detector setup is completely compatible to the standard STEM-EELS technique. In particular, the *on-axis* detector could lead to a strong intensity of EELS signals, benefit to the SNR of EMCD measurement. Significantly, both the in-plane and out-of-plane EMCD signals from the single atomic plane can be extracted by subtracting the chiral EELS signals from  $1/4d$  and  $-1/4d$  ( $3/4d$ ) beam positions after one STEM-EELS scanning. The separation of in-plane and out-of-plane EMCD signals can be simply achieved by shifting the detector positions. Therefore, atomic resolution EMCD for 3D measurement of magnetic moments has been demonstrated. Note that the *on-axis* detector could give pure in-plane EMCD signals as the out-of-plane EMCD signals are totally canceled out owing to its antisymmetric distribution with respect to the  $x$  axis. However, the out-of-plane EMCD signals using an *off-axis* detector are mixed with a small portion of in-plane EMCD signals. Nevertheless, it is estimated to be less than 10% and can be further reduced by moving the detector away from the transmitted beam along the  $y$  axis.

The low signal intensity and SNR are the biggest obstacle for EMCD measurement, which becomes more serious approaching atomic resolution because of the extremely small interaction volume [21,36]. Optimizing the experimental parameters are very practical to solve these issues. As shown in Figs. 2(f) and 2(g), the CA can be optimized to be 15 mrad. In addition, here we propose to use a defocused electron beam to enhance the intensity of EMCD signals. By positioning the electron beam at  $d/4$ , the simulated distributions of in-plane and out-of-plane EMCD signals are shown in Figs. 3(a) and 3(b) as a function of defocus value ( $df$ ), respectively. Remarkably, a certain  $df$  could increase the intensity of EMCD signals. The  $df$  between  $-4$  to  $-8$  nm gives the largest enhancement both for in-plane and out-of-plane EMCD signals, as they share the same dynamical diffraction conditions. The electron beam with positive or very large negative defocus value leads to the reduced intensity of EMCD signals, which can be attributed to the increased delocalization as the electrons might delocalized from  $d/4$  position to  $-d/4$  ( $3d/4$ ) position and thus give to the negative contribution.

Moreover, the contribution of EMCD signals from different depths are calculated in Fig. S1 in the Supplemental Material [35]. Compared to the zero-defocus condition for which only the thickness between 0 and 6 nm give the positive contribution, the whole thickness range from 0 to 10 nm positively contributes to the final EMCD signals at  $df = -8$  nm. Therefore, the defocused electron

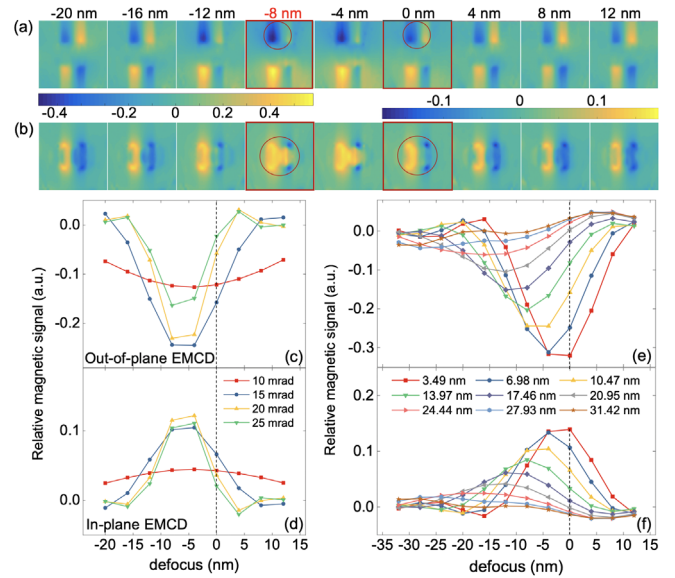


FIG. 3. Enhancing EMCD signals using a defocused electron beam. (a),(b) Simulated distributions of out-of-plane and in-plane EMCD signals by parking the beam at the  $d/4$  position as a function of defocus value, respectively, at  $V = 300$  kV,  $t = 10.47$  nm, and  $CA = 15$  mrad. The extracted EMCD signals from the EELS detectors marked with red circles in (a) as a function of defocus value under different CAs and thickness both for in-plane (d),(f) and out-of-plane (c),(e), respectively. The dotted black lines indicate the defocus value of zero.

beam could redistribute the electrons in the crystal and thus enhance the EMCD signals, similar to the depth sectional STEM technique, while it is used to obtain the depth-resolved magnetic information [37,38].

Furthermore, the EMCD signals at different CA and thickness are calculated as a function of defocus value as shown in Figs. 3(c)–3(f). For the fixed thickness at 10.47 nm in Figs. 3(c) and 3(d), the optimized defocus value is almost independent of CA. The  $CA = 15$  mrad provides the strongest signals at  $df = -4$  nm. With the increasing thickness, the optimized defocus value is increased accordingly from  $df = 0$  nm for  $t = 3.49$  nm to  $df = -12$  nm for  $t = 20$  nm in Figs. 3(e) and 3(f). Owing to the strong dynamical diffraction effects, the intensity of EMCD signals are decayed quickly with respect to the thickness. Particularly, it approaches to zero at 20.95 nm at zero-defocus condition while increased to 0.1 and 0.04 at  $df = -12$  nm for the out-of-plane and in-plane cases, respectively. Therefore, the EMCD signals are saved from the nonmeasurable level and the effective thickness range is extended through introducing the defocused electron beam.

The delocalization of EMCD signals is also discussed. The electron beam is set to scan across six atomic planes. The contribution of EMCD signals from each atom plane are separately calculated in Fig. 4 at  $V = 300$  kV,  $t = 10.47$  nm,  $CA = 15$  mrad, and  $df = -8$  nm. The

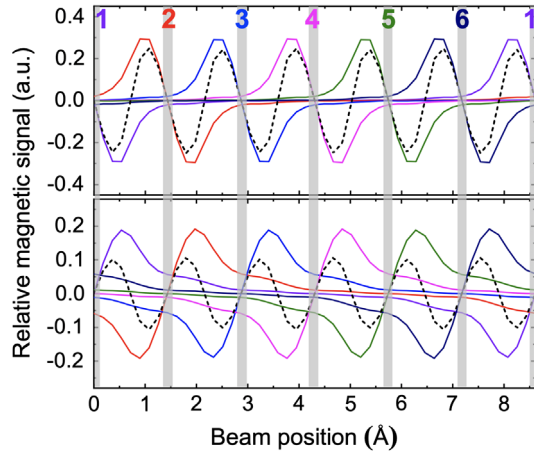


FIG. 4. Delocalization of EMCD signals at atomic resolution. The contribution of EMCD signals from each atomic plane are plotted with colored lines. The total signals are plotted with dotted black lines. The upper and lower panels are for the in-plane and out-of-plane cases, respectively. The gray rectangle boxes indicate the positions of atomic planes.

positions of each atomic plane are indicated with gray rectangle boxes. The total signal (black dotted line) is asymmetric with respect to the atomic plane. Taking as an example atom plane 3, on its left  $1/4d$  position, almost 80% of out-of-plane and 65% in-plane EMCD signals are from atomic plane 3 (blue line). The two nearest planes [atomic plane 2 (red) and 4 (pink)] together give the negative contributions owing to the delocalization of EMCD signals [39]. It is more obvious for the in-plane case while the atomic resolved features are still clear. In addition, we stress that the atomic resolution 3D EMCD is also able to measure the antiferromagnets, e.g., NiO, for which the nearest planes have the opposite spin orientation. Consequently, the nearest planes could give the positive contribution and further enhance the total EMCD signals. Therefore, our method will become even more applicable for antiferromagnets, showing another incomparable advantage over the XMCD technique.

At last, the SNR for 3D EMCD measurement is discussed. Similarly, the definition of SNR for EMCD signals is taken as described in Refs. [21,36–38,40]; that is  $\text{SNR} = f_{\text{red}}(M/N)(\sigma_{\text{Mag}}/\sigma_{\text{Nonmag}})\sqrt{2N_{\text{pix}}C_{L_3}/(1+b)}$ .  $M/N$  is the ratio of intrinsic magnetic and nonmagnetic components determined by the electronic properties of magnetic element.  $\sigma_{\text{Mag}}/\sigma_{\text{Nonmag}}$  is the simulated relative intensity of EMCD signals as shown in Fig. 4.  $N_{\text{pix}}$  is the number of pixel that is used for signal integration, e.g.,  $N_{\text{pix}} = 3 \times 50$  pixel under the three-beam orientation.  $f_{\text{red}}$  is the reduced factor due to the signal integration, e.g.,  $f_{\text{red}} = 0.8$ .  $C_{L_3}$  is the electron counts at  $L_3$  peak after background subtraction.  $b$  is the ratio of the electron counts between EELS background and  $C_{L_3}$ , e.g.,  $b = 2$ . Here, we reasonably take  $C_{L_3} = 1000$  for an *on-axis* EELS detector (in-plane measurement) under the common setup of beam

current and dwell time in standard STEM-EELS experiments as described before [21,36,37], e.g., approximately 100 pA and tens of millisecond per pixel, respectively. While for an *off-axis* EELS detector for out-of-plane EMCD measurement, it is further approximately reduced by a factor of 4 as shown in the Supplemental Material Fig. S2, e.g.,  $C_{L_3} = 250$ . Thus,  $\text{SNR}|_{\text{out-of-plane}} = 31.6(M_z/N)$  and  $\text{SNR}|_{\text{in-plane}} = 25.4(M_y/N)$  by taking the maximum of  $\sigma_{\text{Mag}}/\sigma_{\text{Nonmag}}$  in Fig. 4. Consequently,  $M/N$  should be larger than  $0.10 \sim 0.12$  to obtain  $\text{SNR} > 3$ , comparable to the theoretical value for 3d transition metals. Moreover, the beam current, dwell time and  $N_{\text{pix}}$  can be further increased if the sample is robust against the irradiation damage and the microscope is stable enough. Note that these estimations are conducted with the assumption of pure Poisson noise if the direct electron detectors are used as mentioned before [37]. Fortunately, these kinds of detectors are accessible now [41–43] and might contribute significantly to the 3D EMCD measurement at atomic scale in the future. Moreover, the average of a large number of EEL spectra ( $N_{\text{pix}}$ ) perpendicular to the scanning direction, especially under the three-beam orientation, could further reduce the Poisson noise [44].

Our proposed approach has theoretically extended the EMCD measurement from one dimension to three dimensions at atomic scale, which is a generalization of atomic-plane-resolved (APR) EMCD proposed by Jan Rusz [16] in the STEM mode. Therefore, the compatibility with the STEM-EELS setup makes it more accessible compared to the APR-EMCD based on the unique achromatic electron microscopy in TEM mode [17], especially when an *on-axis* EELS detector is adopted for in-plane magnetic measurement. Recent studies have also demonstrated the method of using a patterned aperture for atomic resolution EMCD measurement in STEM mode [21–23]. However, the fixed shape and size of the patterned EELS aperture might limit its general application. In addition, no shaped electron beam with customized phase distributions are necessary here, in contrast to the vortex beam [18], aberrated electron beam [19,20], and the orbital angular momentum sorter [24].

In summary, we have developed the atomic resolution 3D EMCD to measure the magnetic moment vectors in all three Cartesian directions, which is compatible with the widely spread STEM-EELS setup on aberration corrected microscopes. The out-of-plane and in-plane magnetic moments can be straightforwardly measured just by simply shifting the EELS detector. The method is not only advantaged over the tomographic technique without the highly demanding on experimental tilting series and post reconstruction algorithm, but also over the vortex beam [45] which is only proposed to measure atomic resolution EMCD signals for out-of-plane magnetization [18,34,40,46,47]. Moreover, the introduction of a

defocused electron beam could heavily enhance the intensity of EMCD signals, promising a substantial possibility in future experiments. We believe our method will be achieved on the newly developing atomic resolution magnetic-field-free microscope for ferromagnets as well as antiferromagnets, providing an alternative of magnetic characterization techniques for 3D measurement at the atomic scale.

This project has received funding from the Chinese National Natural Science Foundation (52173215), the Deutsche Forschungsgemeinschaft grant (Project No. 392476493) to support collaboration between Germany and China and the European Research Council (ERC) under the European Union's Horizon 2020 research and innovation programme (Grant No. 856538, project "3D MAGiC"). We thank Dr. Jan Ruzs for providing the MATS v2 software.

---

\*Corresponding author.  
dsong@ahu.edu.cn

- [1] C. Donnelly, M. Guizar-Sicairos, V. Scagnoli, S. Gliga, M. Holler, J. Raabe, and L. J. Heyderman, *Nature (London)* **547**, 328 (2017).
- [2] C. Donnelly, S. Finizio, S. Gliga, M. Holler, A. Hrabec, M. Odstrčil, S. Mayr, V. Scagnoli, L. J. Heyderman, M. Guizar-Sicairos, and J. Raabe, *Nat. Nanotechnol.* **15**, 356 (2020).
- [3] C. Phatak, A. K. Petford-Long, and M. De Graef, *Phys. Rev. Lett.* **104**, 253901 (2010).
- [4] D. Wolf, L. A. Rodriguez, A. Béch e, E. Javon, L. Serrano, C. Magen, C. Gatel, A. Lubk, H. Lichte, S. Bals, G. Van Tendeloo, A. Fern andez-Pacheco, J. M. De Teresa, and E. Snoeck, *Chem. Mater.* **27**, 6771 (2015).
- [5] P. Simon, D. Wolf, C. Wang, A. A. Levin, A. Lubk, S. Sturm, H. Lichte, G. H. Fecher, and C. Felser, *Nano Lett.* **16**, 114 (2016).
- [6] D. Wolf, N. Biziere, S. Sturm, D. Reyes, T. Wade, T. Niermann, J. Krehl, B. Warot-Fonrose, B. B uchner, E. Snoeck, C. Gatel, and A. Lubk, *Commun. Phys.* **2**, 87 (2019).
- [7] C. H ebert and P. Schattschneider, *Ultramicroscopy* **96**, 463 (2003).
- [8] P. Schattschneider, S. Rubino, C. H ebert, J. Ruzs, J. Kuneš, P. Nov ak, E. Carlino, M. Fabrizioli, G. Panaccione, and G. Rossi, *Nature (London)* **441**, 486 (2006).
- [9] P. Schattschneider, C. H ebert, S. Rubino, M. St oger-Pollach, J. Ruzs, and P. Nov ak, *Ultramicroscopy* **108**, 433 (2008).
- [10] P. Schattschneider, M. St oger-Pollach, S. Rubino, M. Sperl, C. Hurm, J. Zweck, and J. Ruzs, *Phys. Rev. B* **78**, 104413 (2008).
- [11] S. Muto, J. Ruzs, K. Tatsumi, R. Adam, S. Arai, V. Kocovski, P. M. Oppeneer, D. E. B urgler, and C. M. Schneider, *Nat. Commun.* **5**, 3138 (2014).
- [12] T. Thersleff, J. Ruzs, B. Hj orvarsson, and K. Leifer, *Phys. Rev. B* **94**, 134430 (2016).
- [13] T. Thersleff, S. Muto, M. Werwiński, J. Spiegelberg, Y. Kvashnin, B. Hj orvarsson, O. Eriksson, J. Ruzs, and K. Leifer, *Sci. Rep.* **7**, 44802 (2017).
- [14] S. Schneider, D. Pohl, S. L offler, J. Ruzs, D. Kasinathan, P. Schattschneider, L. Schultz, and B. Rellinghaus, *Ultramicroscopy* **171**, 186 (2016).
- [15] D. Song, L. Ma, S. Zhou, and J. Zhu, *Appl. Phys. Lett.* **107**, 042401 (2015).
- [16] J. Ruzs, S. Muto, J. Spiegelberg, R. Adam, K. Tatsumi, D. E. B urgler, P. M. Oppeneer, and C. M. Schneider, *Nat. Commun.* **7**, 12672 (2016).
- [17] Z. Wang, A. H. Tavabi, L. Jin, J. Ruzs, D. Tyutyunnikov, H. Jiang, Y. Moritomo, J. Mayer, R. E. Dunin-Borkowski, R. Yu, J. Zhu, and X. Zhong, *Nat. Mater.* **17**, 221 (2018).
- [18] J. Ruzs and S. Bhowmick, *Phys. Rev. Lett.* **111**, 105504 (2013).
- [19] J. Ruzs, J.-C. Idrobo, and S. Bhowmick, *Phys. Rev. Lett.* **113**, 145501 (2014).
- [20] J. C. Idrobo, J. Ruzs, J. Spiegelberg, M. A. McGuire, C. T. Symons, R. R. Vatsavai, C. Cantoni, and A. R. Lupini, *Adv. Struct. Chem. Imaging* **2**, 5 (2016).
- [21] D. Negi, J. Spiegelberg, S. Muto, T. Thersleff, M. Ohtsuka, L. Sch onstr om, K. Tatsumi, and J. Ruzs, *Phys. Rev. Lett.* **122**, 037201 (2019).
- [22] H. Ali, D. Negi, T. Warnatz, B. Hj orvarsson, J. Ruzs, and K. Leifer, *Phys. Rev. Research* **2**, 023330 (2020).
- [23] T. Thersleff, L. Sch onstr om, C.-W. Tai, R. Adam, D. E. B urgler, C. M. Schneider, S. Muto, and J. Ruzs, *Sci. Rep.* **9**, 18170 (2019).
- [24] E. Rotunno, M. Zanfrognini, S. Frabboni, J. Ruzs, R. E. Dunin Borkowski, E. Karimi, and V. Grillo, *Phys. Rev. B* **100**, 224409 (2019).
- [25] J. Ruzs, O. Eriksson, P. Nov ak, and P. M. Oppeneer, *Phys. Rev. B* **76**, 060408(R) (2007).
- [26] L. Calmels, F. Houdellier, B. Warot-Fonrose, C. Gatel, M. J. H ytch, V. Serin, E. Snoeck, and P. Schattschneider, *Phys. Rev. B* **76**, 060409(R) (2007).
- [27] H. Lidbaum, J. Ruzs, A. Liebig, B. Hj orvarsson, P. M. Oppeneer, E. Coronel, O. Eriksson, and K. Leifer, *Phys. Rev. Lett.* **102**, 037201 (2009).
- [28] Z. Q. Wang, X. Y. Zhong, R. Yu, Z. Y. Cheng, and J. Zhu, *Nat. Commun.* **4**, 1395 (2013).
- [29] D. Song, G. Li, J. Cai, and J. Zhu, *Sci. Rep.* **6**, 18489 (2016).
- [30] J. Ruzs, S. Rubino, O. Eriksson, P. M. Oppeneer, and K. Leifer, *Phys. Rev. B* **84**, 064444 (2011).
- [31] D. Song, A. H. Tavabi, Z.-A. Li, A. Kov acs, J. Ruzs, W. Huang, G. Richter, R. E. Dunin-Borkowski, and J. Zhu, *Nat. Commun.* **8**, 15348 (2017).
- [32] N. Shibata, Y. Kohno, A. Nakamura, S. Morishita, T. Seki, A. Kumamoto, H. Sawada, T. Matsumoto, S. D. Findlay, and Y. Ikuhara, *Nat. Commun.* **10**, 2308 (2019).
- [33] J. Ruzs, *Ultramicroscopy* **177**, 20 (2017).
- [34] J. Ruzs, S. Bhowmick, M. Eriksson, and N. Karlsson, *Phys. Rev. B* **89**, 134428 (2014).
- [35] See Supplemental Material at <http://link.aps.org/supplemental/10.1103/PhysRevLett.127.087202> for the descriptions of EMCD signals, the details of EMCD simulation procedures and parameters, the contribution of EMCD

- signals from different depths to total EMCD signals at different defocus values, nonmagnetic and magnetic signals as a function of beam position for Fig. 4, respectively.
- [36] J. Ruzs and J. C. Idrobo, *Phys. Rev. B* **93**, 104420 (2016).
- [37] D. Negi, P. M. Zeiger, L. Jones, J.-C. Idrobo, P. A. van Aken, and J. Ruzs, *Phys. Rev. B* **100**, 104434 (2019).
- [38] D. Negi, L. Jones, J.-C. Idrobo, and J. Ruzs, *Phys. Rev. B* **98**, 174409 (2018).
- [39] J. Ruzs, J. Spiegelberg, S. Muto, T. Thersleff, M. Ohtsuka, K. Leifer, and P. M. Oppeneer, *Phys. Rev. B* **95**, 174412 (2017).
- [40] D. S. Negi, J. C. Idrobo, and J. Ruzs, *Sci. Rep.* **8**, 4019 (2018).
- [41] A. Maigné and M. Wolf, *Microscopy* **67**, i86 (2018).
- [42] J. L. Hart, A. C. Lang, A. C. Leff, P. Longo, C. Trevor, R. D. Twosten, and M. L. Taheri, *Sci. Rep.* **7**, 8243 (2017).
- [43] B. Plotkin-Swing, G. J. Corbin, S. De Carlo, N. Dellby, C. Hoermann, M. V. Hoffman, T. C. Lovejoy, C. E. Meyer, A. Mittelberger, R. Pantelic, L. Piazza, and O. L. Krivanek, *Ultramicroscopy* **217**, 113067 (2020).
- [44] P. Cueva, R. Hovden, J. A. Mundy, H. L. Xin, and D. A. Muller, *Microsc. Microanal.* **18**, 667 (2012).
- [45] J. Verbeeck, H. Tian, and P. Schattschneider, *Nature (London)* **467**, 301 (2010).
- [46] D. Pohl, S. Schneider, P. Zeiger, J. Ruzs, P. Tiemeijer, S. Lazar, K. Nielsch, and B. Rellinghaus, *Sci. Rep.* **7**, 934 (2017).
- [47] P. Schattschneider, S. Löffler, M. Stöger-Pollach, and J. Verbeeck, *Ultramicroscopy* **136**, 81 (2014).